Laser and Particle Beams (2001), *19*, 579–595. Printed in the USA.

DOI: 10.1017.S026303460119405X

Measurement and analysis of gas-puff density distributions for plasma radiation source *z* pinches

D. MOSHER,[1] B.V. WEBER,[1] B. MOOSMAN,[1] R.J. COMMISSO,[1] P. COLEMAN,[2] E. WAISMAN,[2] H. SZE,[2] Y. SONG,[2] D. PARKS,[2] P. STEEN,[2] J. LEVINE,[2] B. FAILOR,[2] AND A. FISHER[2]

[1]Pulsed Power Physics Branch, Plasma Physics Division, Naval Research Laboratory, Washington, DC 20375-5346, USA
[2]Maxwell Physics International, San Leandro, CA 94577-0599, USA

(RECEIVED 22 May 2000; ACCEPTED 22 February 2001)

Abstract

High-sensitivity interferometry measurements of initial density distributions are reviewed for a wide range of gas-puff nozzles used in plasma radiation source (PRS) *z*-pinch experiments. Accurate gas distributions are required for determining experimental load parameters, modeling implosion dynamics, understanding the radiation properties of the stagnated pinch, and for predicting PRS performance in future experiments. For a number of these nozzles, a simple ballistic-gas-flow model (BFM) has been used to provide good physics-based analytic fits to the measured *r*, *z* density distributions. These BFM fits provide a convenient means to smoothly interpolate radial density distributions between discrete axial measurement locations for finer-zoned two-dimensional MHD calculations, and can be used to determine how changes in nozzle parameters and load geometry might alter implosion dynamics and radiation performance. These measurement and analysis techniques are demonstrated for a nested-shell nozzle used in Double Eagle and Saturn experiments. For this nozzle, the analysis suggests load modifications that may increase the *K*-shell yield.

1. INTRODUCTION

A high-sensitivity laser interferometer (Weber & Fulghum, 1997) has been used to measure gas density distributions from a wide variety of nozzles used in plasma radiation source (PRS) *z*-pinch experiments (Deeney *et al*., 1993; Coverdale *et al*., 1996; Sanford *et al*., 1996*a*; Coleman *et al*., 1997; Weber *et al*., 1997, 1999*a*; Commisso *et al*., 1998; Levine *et al*., 1998, 2000; Moosman *et al*., 1999*a*; Sze *et al*., 1999; Shishlov *et al*., 2000; Song *et al*., 2000). These gas-puff loads provide intense sources of *K*-shell X-radiation not accessible with wire arrays (Deeney *et al*., 1995, 1998; Sanford *et al*., 1996*b*; Spielman *et al*., 1997), and their naturally diffuse mass distributions may provide mediation of the Raleigh–Taylor (RT) instability (Gol'berg & Velikovich, 1993; Hammer *et al*., 1996; Coleman *et al*., 1997; Deeney *et al*., 1998; Velikovich *et al*., 1998*a*, 1998*b*; Shishlov *et al*., 2000) believed to be endemic to large-radius PRS loads. Accurate gas distributions are required for determining experimental load parameters, modeling implosion dynamics, understanding the radiation properties of the stagnated pinch, and for predicting PRS performance in future experiments. These measurements indicate how changes in pressure and timing in experiments affect the initial mass distribution. Specific nozzle designs can be tested and modified to obtain desired gas distributions, and gas-dynamics codes used for nozzle design can be benchmarked against interferometer data.

The density distribution in the load region is determined by integrating the gas density along a horizontal laser-beam line of sight as a function of time at one axial distance from the nozzle and one vertical distance from the symmetry axis. The nozzle is moved in steps to cover the gas-distribution cross section, and the measurements are Abel-inverted to compute the local density $n(r, z, t)$. Several examples are shown to illustrate the technique. In addition to neutral-gas *r*–*z* distribution measurements, the instrument has been used to determine the azimuthal symmetry of tested nozzles and to measure the preimplosion ionization distribution produced by an intense ultraviolet (UV) flashboard source.

A simple ballistic-gas-flow model (BFM) has been used to provide good physics-based analytic fits to the measured *r*–*z* density distributions of several nozzles. These BFM fits provide a convenient means to smoothly interpolate radial density distributions between discrete axial measurement locations for finer-zoned two-dimensional MHD calculations. The BFM can also be used to determine how changes in nozzle parameters and load geometry might alter implosion dynamics and radiation performance.

Address correspondence and reprint requests to: D. Mosher, Code 6770, Naval Research Laboratory, 4555 Overlook Ave., S.W., Washington, DC 20375-5346. E-mail: mosher@suzie.nrl.navy.mil

The utility of the BFM is demonstrated in an analysis of long-implosion-time argon nested-shell, or shell-on-shell (SOS) gas-puff experiments on the Maxwell Physics International (MPI) Double Eagle (DE) generator (Sze *et al.*, 1999). The goal of such experiments is to achieve efficient *K*-shell radiation production with slower and less-expensive pulsed-power drivers. The 200-ns implosion times of these experiments require larger-radius (and more R-T-unstable) loads than used with 100-ns drivers to achieve the high implosion velocities (low load masses) needed for optimal *K*-shell radiation production (Thornhill *et al*., 1996; Mosher *et al*., 1998). Argon *K*-shell yields from large-radius implosions on the GIT-12 generator have been shown to increase dramatically due to R-T mitigation when double-shell argon gas puffs replaced single shells (Shishlov *et al*., 2000). For the DE analysis, radial snowplow computations at various axial locations are combined with a two-level radiation model (Mosher *et al*., 1998) to predict the *K*-shell yield as a function of *z*. Both this analysis and the experiment show increased yield per centimeter with increased distance from the nozzle, suggesting that modified gas-puff-nozzle characteristics may achieve an increase in overall *K*-shell yield by boosting yield per centimeter close to the nozzle. Simple nozzle modifications are suggested that indicate a substantial calculated yield increase.

2. GAS DISTRIBUTION MEASUREMENTS

Gas distributions from PRS nozzles are measured using high-sensitivity laser interferometry (Weber & Fulghum, 1997) with the arrangement illustrated in Figure 1. The shaded region represents a generic, azimuthally-symmetric gas (and/or free-electron) distribution centered at the origin of a cartesian coordinate system with the axis of symmetry along *z* and the *x*–*y* plane parallel to the face of the gas nozzle. Gas emerging from the nozzle propagates primarily in the *z* direction. Two c. w. laser beams with wavelength $\lambda = 532$ (GR) and 1064 (IR) nm are each split into two beams, one traversing the gas (scene beam) and one traversing vacuum (reference beam). The two scene beams can be aligned along the same path through the gas for simultaneous, two-color interferometry. For gas-only measurements, single-color interferometry is sufficient. The two-color technique is useful when, as discussed below for gas ionized by a UV source, distinct gas and free-electron distributions are to be measured.

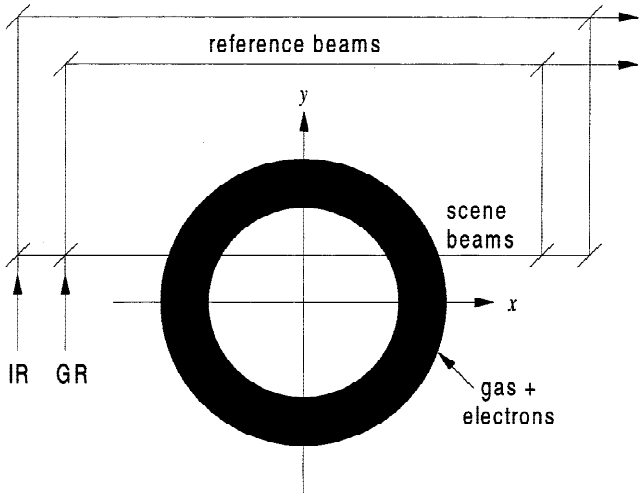

Fig. 1. Optical arrangement for two-color interferometry.

When the scene beam traverses gas, its phase velocity is reduced because the index of refraction is greater than 1. The beams are recombined using optics and detection electronics that are configured to directly measure the sine of the phase difference between the reference and scene beams as a function of time. The line-integral of the gas density N_L is directly proportional to the measured phase shift $\Delta\phi$ (radians)

$$N_L(y) \equiv \int_{-\infty}^{\infty} n(r)\,dx = \frac{\lambda}{2\pi}\,\frac{n_0}{\nu - 1}\,\Delta\phi, \tag{1}$$

where n is the density at radius $r = \sqrt{x^2 + y^2}$, and ν is the index of refraction at density n_0. For argon, the line-integrated density is given by

$$N_L(\mathrm{cm}^{-2}) = 2.7 \times 10^{13}\lambda(\mathrm{nm})\Delta\phi(^\circ). \tag{2}$$

Sophisticated vibration isolation provides a phase-shift sensitivity of $10^{-4}\lambda$ (0.036°) for time scales of 1 ms or less. This high sensitivity allows measurements of low line densities (above about 5×10^{14} cm^{-2} for the green beam), such as those in the important low-density region around the periphery of a gas puff. Typical maximum argon line densities are 10^{18} cm^{-2} or greater, resulting in green-beam phase shifts of 70° or more. The dynamic range of the line-density measurements can therefore be 2000 or more. Measurement precision decreases as the phase shift approaches 180°. The IR beam is used for cases where the line-integrated density is too large to be measured accurately using the green beam, doubling the range for accurate measurements. Line-integrated density is measured as a function of time at one distance *y* from the nozzle axis, and the standard deviation of multiple measurements is used as an estimate of the uncertainty ΔN_L. This uncertainty is usually determined by the shot-to-shot reproducibility of the valve/nozzle system and not the interferometer.

Many important gas flow parameters can be derived from line-density measurements. Their derivation will be illustrated using data obtained with the MPI SOS nozzle fielded on DE and the Sandia National Laboratories (SNL) Saturn generator (Sze *et al*., 1999). This nozzle is chosen as an example because the density distribution is more complex than for other cases, and because modeling based on the gas-distribution measurements has been benchmarked against the DE experiments (Sects. 4 and 5).

https://doi.org/10.1017/S026303460119405X Published online by Cambridge University Press

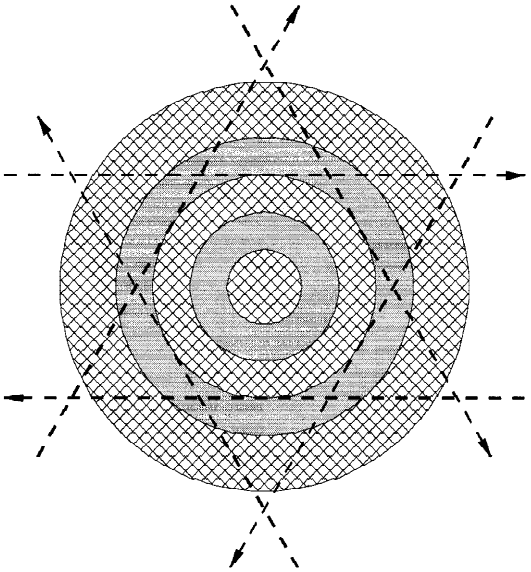

Fig. 2. Laser lines of sight for azimuthal symmetry tests at $z = 0.2$ cm.

2.1. Azimuthal symmetry

It is desirable for the gas distribution to be as azimuthally symmetric as possible. Azimuthal asymmetry will limit the stagnation radius of the implosion (Mosher, 1994) and therefore reduce the X-ray yield. A high degree of symmetry is also a practical concern for interferometry in order to accurately determine the radial dependence of the gas density from an Abel-inversion of the line-integrated density.

The azimuthal symmetry of the SOS nozzle was tested by measuring line densities along the six lines of sight illustrated in Figure 2. The cross-hatched regions in the figure are the metal surfaces at the exit plane of the SOS nozzle. The annular shaded regions are the concentric gas nozzle apertures. The inner and outer radii of the inner-shell aperture are 1 and 2 cm; the radii of the outer-shell aperture are 3 and 4 cm. The two shells are supplied by independent plenums, so that the gas constituents and their pressures can be different. Both plenums are exhausted into the nozzles at the same time using a fast valve. A breakdown pin is installed in the outer shell to provide a timing fiducial to synchronize gas flow with the pulsed-power generator. For the measurements reported here, the breakdown pin determines time zero.

The lines of sight in Figure 2 were obtained by rotating the nozzle in 60° increments inside a vacuum test chamber while keeping the laser beam horizontal. The lines of sight were located at $z = 0.2$ cm from the nozzle, where thin gas annuli from the two nozzles are well separated. Each line of sight samples an azimuthal section of the outer shell as shown. For each line of sight, three line-density measurements were averaged. The line-density data obtained with 10-psia argon in both plenums are plotted in Figure 3. The redundant measurement sets at 0° and at ±180° indicate that the gas flow and measurement techniques are highly reproducible. The gas is first detected at this axial location about 150 μs after the breakdown pin signal at $t = 0$. The line densities increase to a plateau level of about 6.5×10^{17} cm^{-2} after an additional 850 μs. A typical timing used in experiments is $t = 500$ μs as indicated in Figure 3. At this time, the gas distribution of the outer shell is highly symmetric. The

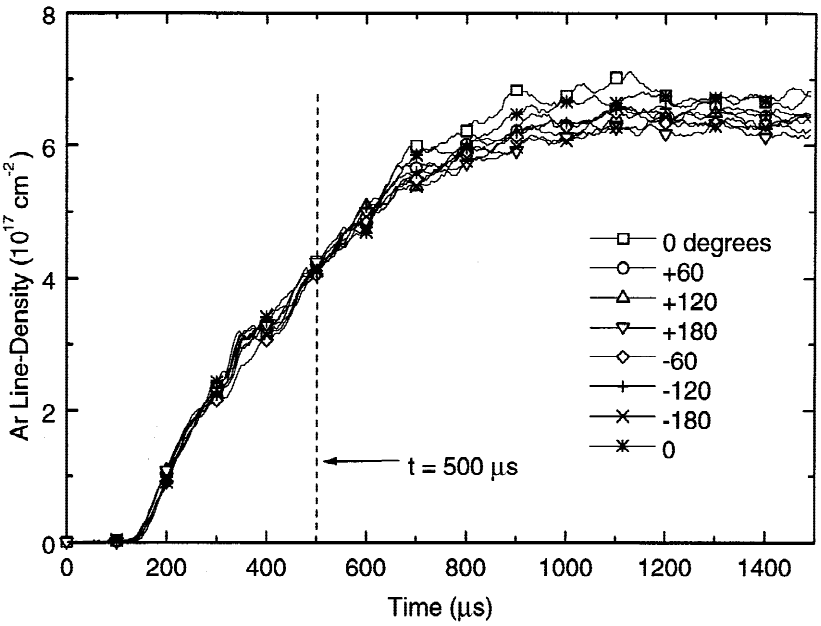

Fig. 3. Azimuthal symmetry data at $y = 3$ cm, $z = 0.2$ cm.

https://doi.org/10.1017/S026303460119405X Published online by Cambridge University Press

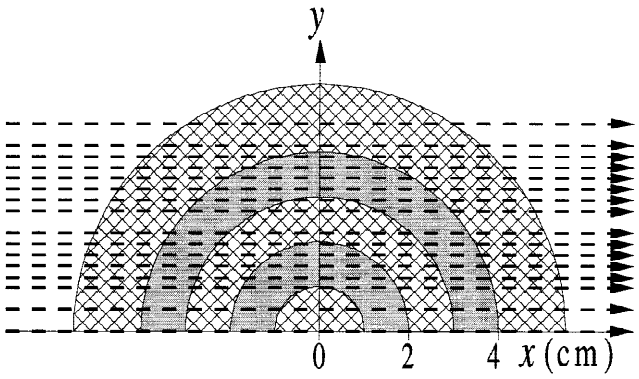

Fig. 4. Laser lines of sight for radial line-density scan at $z = 0.2$ cm.

increased asymmetry at later times may indicate that implosion quality would degrade for these conditions. In what follows, the gas distribution is assumed to be azimuthally symmetric.

2.2. Radial gas distributions

The nozzle is moved vertically inside the vacuum test chamber to measure $N_L(y)$ at enough y locations to determine the radial gas distribution. The local density $n(r)$ is computed (assuming azimuthal symmetry) by Abel inversion from

$$n(r) = -\frac{1}{\pi}\int_r^\infty \frac{dN_L}{dy}\frac{dy}{\sqrt{y^2 - r^2}} \pm \Delta n. \qquad (3)$$

The uncertainty in the density Δn is determined by propagating the measurement error ΔN_L through Eq. (3).

The lines of sight used to determine $n(r)$ at $z = 0.2$ cm for the SOS nozzle with 10 psia in each nozzle are illustrated in Figure 4. The outermost y value is determined empirically to be where the line-integrated density drops to within the measurement sensitivity. The $N_L(t)$ data for these lines of sight are plotted in Figure 5. For $y < 2$ cm, the laser beam probes both shells. For $y > 2$ cm, only the outer shell is probed. The data indicate that the gas emerges simultaneously from the two nozzles, but that they have different rise times. This phenomenon has been attributed to the peculiarities of the valve mechanism (Song *et al*., 2000).

The line-density data at $t = 500$ μs are plotted versus y in Figure 6 (square symbols). The error bars represent plus or minus one standard deviation of ΔN_L determined from the three measurements. The data are converted to the local density $n(r)$ by connecting the $N_L(y)$ points with cubic-spline polynomials subject to $dN_L/dy = 0$ at $y = 0$ and $y = y_0$, where y_0 is the outer-boundary point. Equation (3) can then be solved analytically. The resulting density distribution is also shown in Figure 6 (circles). The $n(r)$ plot shows two separated shells centered in the nozzle apertures. The density error is estimated from a piece-wise linear fit to the line-density measurements, providing a straightforward means to propagate ΔN_L through Eq. (3) to determine Δn. The error in density tends to increase as the radius decreases, because more measurements are involved in the inversion calculation. The nonzero density at $r = 0$ in Figure 6 may be a result of imperfect symmetry or an underestimate of the error. Separate measurements of the inner and outer density distributions give almost exactly the same results as in Figure 6, an indication that the Abel inversion algorithm is able to "see" the inner shell using measurements that probe both shells, and that the quality of the data

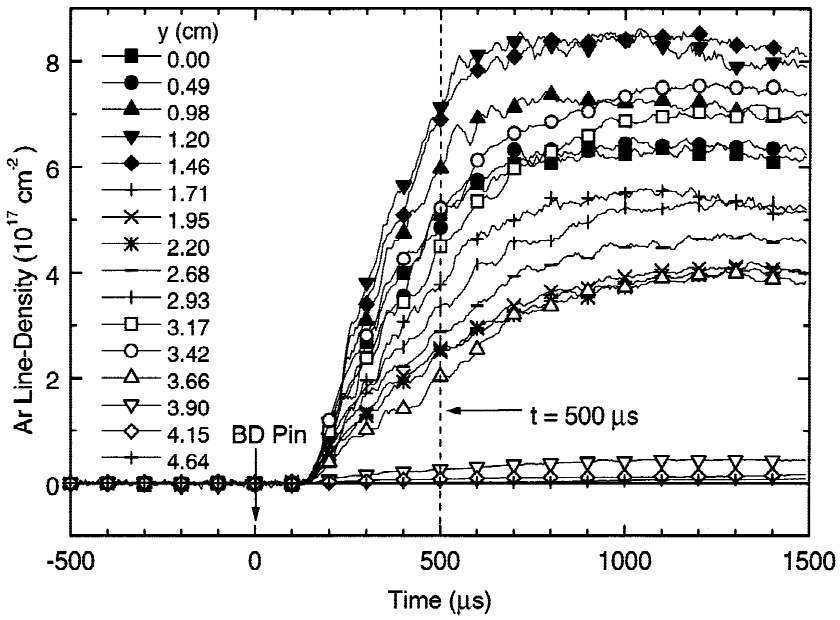

Fig. 5. Line-integrated-density measurements at $z = 0.2$ cm from the nozzle.

https://doi.org/10.1017/S026303460119405X Published online by Cambridge University Press

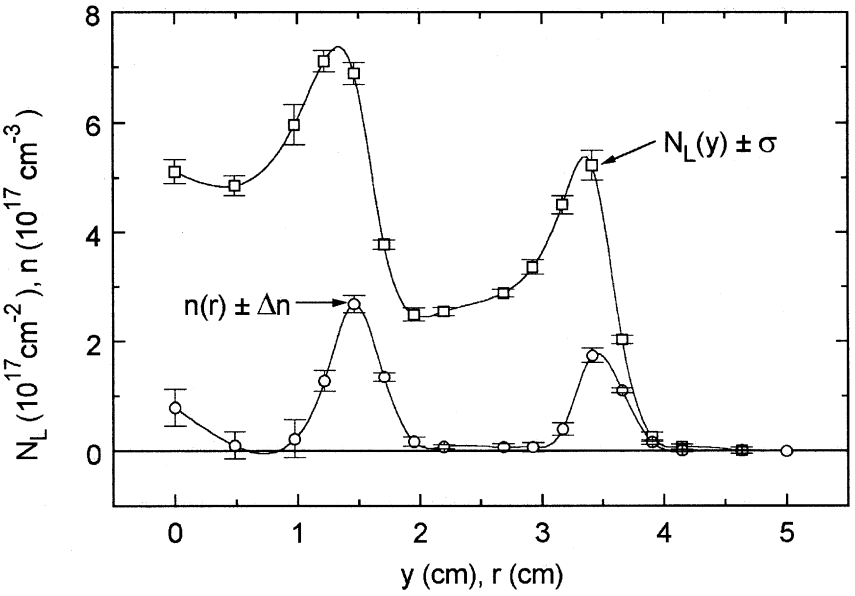

Fig. 6. Line-integrated-density measurements (N_L) and standard deviations (σ) at $t = 500$ μs. Derived density $n(r)$ and error estimate Δn.

and reproducibility of the valve/nozzle system is sufficient to obtain meaningful data.

An r–z cross section of the SOS nozzle is shown in Figure 7 along with the measurement lines of sight. Each nozzle is tilted 5° towards the axis of symmetry as indicated by the dashed lines from the "throats" (the radial constrictions at the start of each nozzle) through the center radius of the exit apertures. Radial gas distributions were determined at three distances from the nozzle: $z = 0.2$, 2.0, and 3.8 cm. These distances were chosen to map the density at locations relevant to recent DE experiments with 4-cm-long loads (Sze *et al*., 1999). The resulting density distributions are plotted in Figure 8. At $z = 2$ cm, the two shells are starting to overlap at $r = 2.5$ cm. At $z = 3.8$ cm, the overlap is more significant. The peak density associated with each nozzle decreases with distance and moves to smaller radius, consistent with the inward tilt angle. The density on the axis is essentially zero for all three distances.

The density distribution varies substantially with distance from the nozzle, changing from two separated annuli close to the nozzle to a slowly varying, diffuse distribution 3.8 cm from the nozzle. The two-dimensional nature of the gas distribution results from radial expansion of the gas out of the nozzles. Analytic fits to these distributions in Section 3 are used to model implosions and radiation production in Sections 4 and 5.

2.3. Mass loading and pressure scaling

The mass per unit length m (g/cm) is determined from the line-density measurements using

$$m = 2m_{\mathrm{Ar}} \int_0^\infty N_L \, dy, \tag{4}$$

where m_{Ar} is the mass of an argon atom. Equation (4) is more precise than an algorithm based on the derived $n(r)$ values. The mass loading for the SOS nozzle is plotted in Figure 9 for 10-psia argon in both plenums. At a typical timing ($t = 500$ μs) used in experiments, the mass varies from 221 μg/cm close to the nozzle to 177 μg/cm at 3.8 cm from the nozzle. This axial mass gradient is the result of operating during the rise of the gas density and time-of-flight considerations: Lower masses at larger values of z reflect reduced-mass emission from the nozzle at earlier times. The axial mass gradient varies with timing and, as shown in Section 5, can be an important gas-puff-load parameter for optimizing PRS performance.

The plenum pressure for the SOS nozzle has been varied from 5 to 40 psia to determine how mass loading scales with

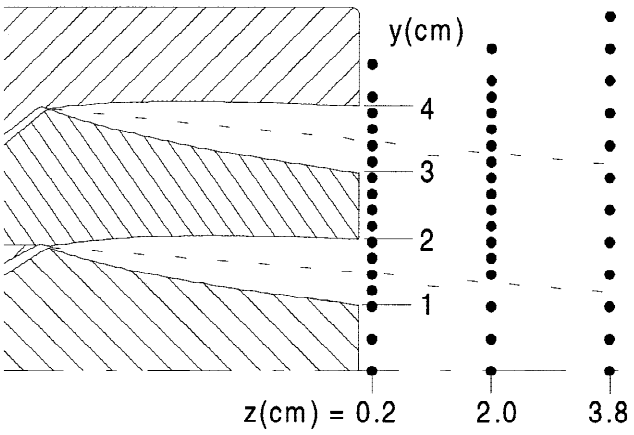

Fig. 7. Laser lines of sight in y–z plane.

https://doi.org/10.1017/S026303460119405X Published online by Cambridge University Press

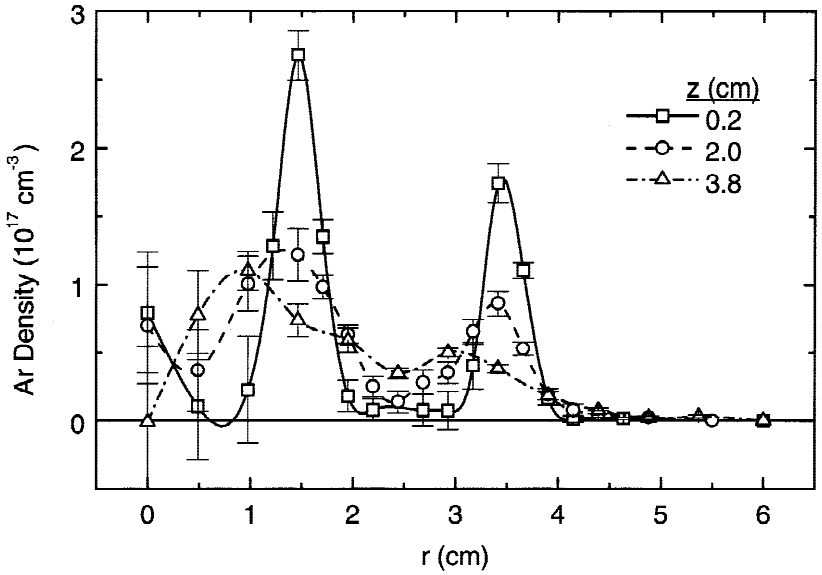

Fig. 8. Radial density distributions ($t = 500$ μs, 10 psia) for three distances from the nozzle.

pressure. Higher-pressure measurements were required to determine load characteristics for the higher currents of Saturn. For this study, the density is not mapped over the cross section. Instead, the line-integrated density is measured at $z = 0.2$ cm, and $y = 0$. To a good approximation, this line-integrated density through the axis of symmetry is proportional to the mass per unit length. The mass is proportional to pressure in the 5- to 20-psia range. For 20–40 psia, the mass is proportional to $(\text{pressure})^{0.9}$. This scaling information can be used to construct density distributions for any pressure in the range based on the detailed density maps measured at 10 psia.

2.4. Preionization

Preionization may be important to improve gas-puff *z*-pinch implosion quality by providing a high-conductivity region on the periphery of the gas for azimuthally symmetric current initiation (Weber *et al*., 1998; Rousskikh *et al*., 1999). In addition, experiments with double-shell nozzles on GIT-4 at the High Current Electronics Institute, Tomsk, Russia (HCEI) indicated the importance of preionization for preventing premature current flow in the inner shell (Baksht *et al*., 1997). An intense-UV flashboard source was developed at the Naval Research Laboratory (NRL) for gas-puff

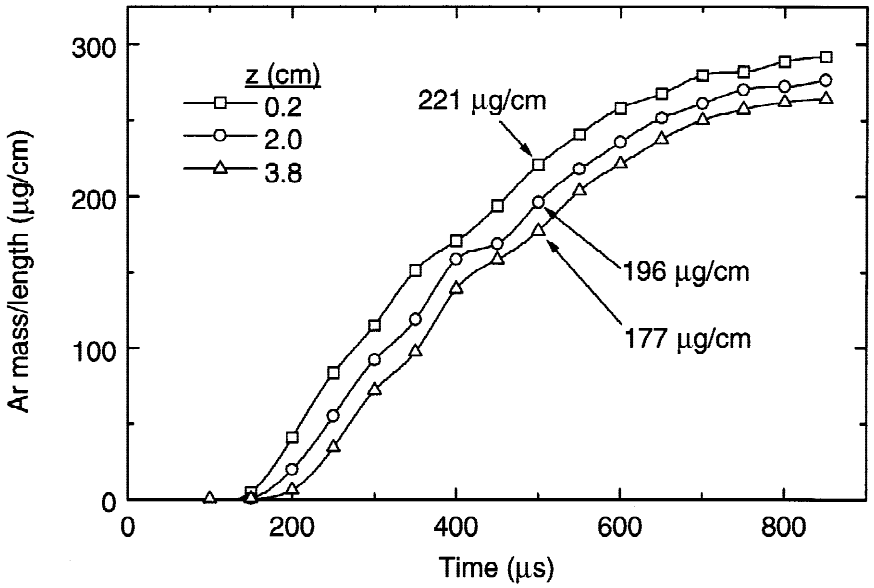

Fig. 9. Mass per unit length derived from the line-integrated-density measurements at three distances from the nozzle.

https://doi.org/10.1017/S026303460119405X Published online by Cambridge University Press

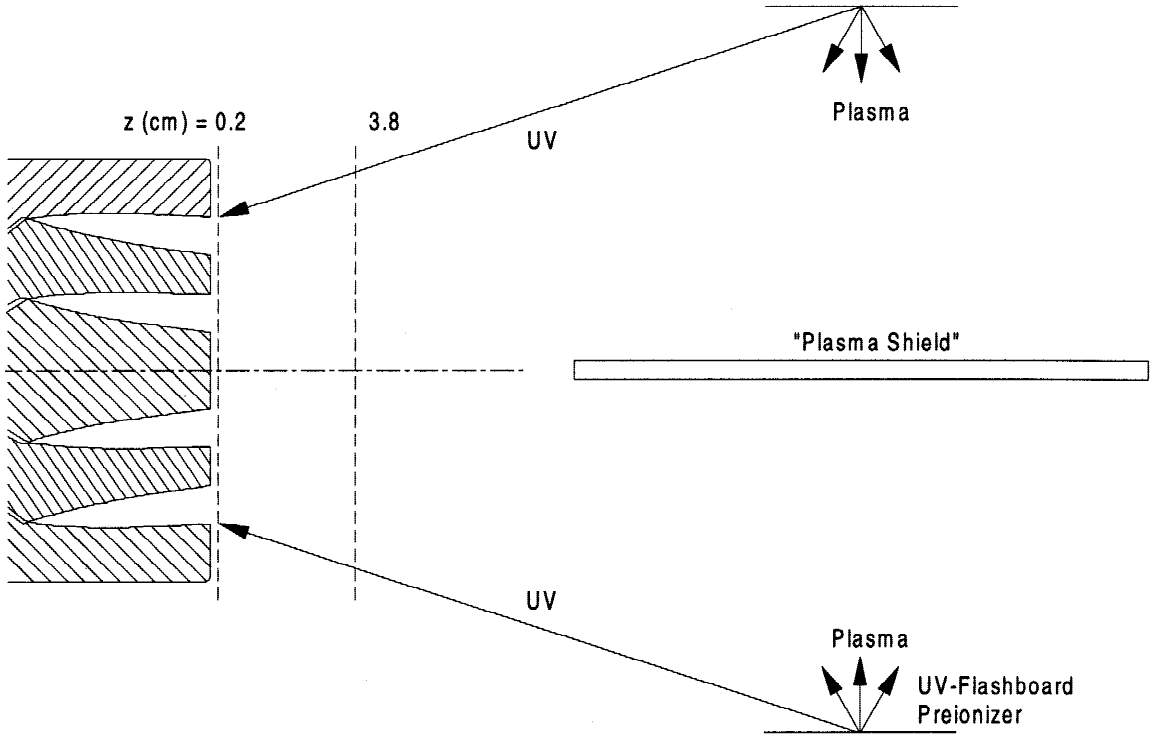

Fig. 10. Preionization arrangement for the SOS nozzle. The UV-flashboards are semicircular strips of electrode gaps with a rectangular "plasma shield" along the diameter between the two flashboards to prevent interaction of their plasmas. The flashboard diameter is 19 cm. The distance from the nozzle to the center of the flashboard circle is 17 cm.

preionization (Weber *et al*., 1998; Moosman *et al*., 1999*a*). The configuration used to measure the preionization of the SOS nozzle is shown in Figure 10. Two semicircular flashboard strips are each powered by a 1.8-μF capacitor bank charged to 22 kV, producing a damped sinusoidal current with 50-kA amplitude and 4-μs period. The flashboard ring is located 17 cm from the nozzle, far enough to delay arrival of plasma to the PRS region until after implosion, yet close enough for sufficient UV intensity to significantly ionize the gas. Plasmas from the flashboards propagate toward the axis of the flashboard circle with typical velocity of a few centimeters per microsecond. The plasma density in the PRS region is negligible for the first 3 μs after firing the capacitors. The intense UV radiation that reaches the periphery of the gas distribution promptly photoionizes the gas.

The interferometer is used in either the two-color or single-color mode to measure the plasma and gas densities (Moosman et al., 1999*a*). The radial distributions of the electron and gas densities for the SOS nozzle at $z = 0.2$ cm are shown in Figure 11. The flashboards were fired 400 μs after the breakdown-pin fiducial. The ionization 3 μs later is a hollow shell on the outer 0.5 cm of the gas distribution. The maximum ionization is about 3%. The ionizing radiation does not penetrate into the inner shell, consistent with photoionization cross sections and the density profiles. At $z =$ 3.8 cm, the gas density distribution is more diffuse (see Fig. 8), allowing penetration of UV and significant ionization into about $r = 2.5$ cm. At this location, the ionization is 10–20% in the $r = 4.5$–5 cm region.

2.5. Review of PRS nozzles and representative gas distributions

The measurement technique and analyses described above have been used at NRL since 1995 to measure gas distributions used in many PRS experiments. The nozzles diagnosed in this way are listed in Table 1. Each nozzle is identified by the laboratory responsible for its development, the generator(s) on which it was fielded, the generic type of gas distribution (annular, solid, or double-shell), the inner diameter (ID) and outer diameter (OD) of the nozzle(s) at the exit plane, the gas used, and relevant references to gas measurements or PRS experiments.

The 18 nozzles listed in Table 1 encompass a large variety of PRS experimental conditions. Based on measured gas distributions, the nozzles can be organized into four general categories to illustrate their major differences. Single-shell annular gas nozzles are represented by two categories, those with "shaped" nozzles (numbers 2, 4–6, 11–13, 15) and those with short, narrow nozzles (numbers 1, 8–10). The third nozzle category includes those that are designed to produce "solid" (well filled-in) gas distributions (numbers 3, 7, 14, 16). The fourth category includes double-shell nozzles (numbers 17, 18).

https://doi.org/10.1017/S026303460119405X Published online by Cambridge University Press

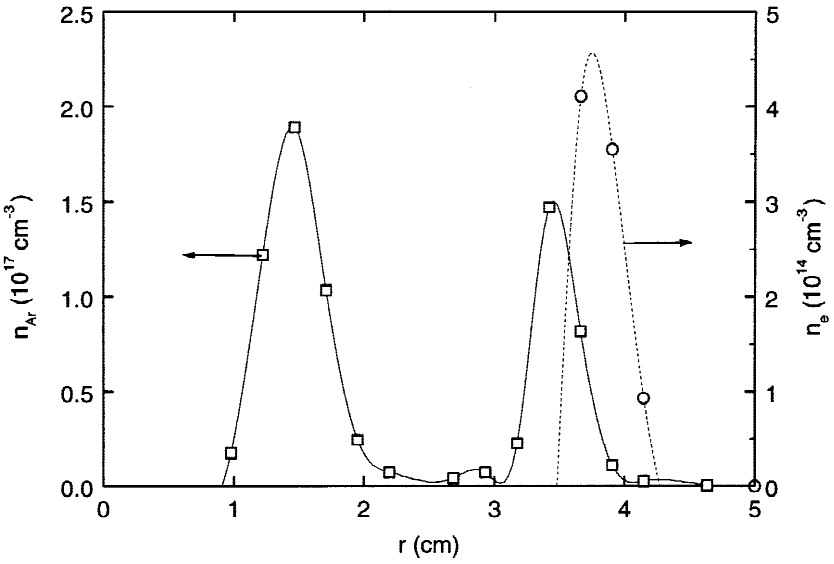

Fig. 11. Gas (n_{Ar}, squares) and electron (n_e, circles) density distributions at $z = 0.2$ cm resulting from pre-ionization, 3 μs after flashboard trigger and 400 μs after breakdown pin.

Table 1. *Gas-puff nozzles used in z-pinch research for which gas density distributions have been measured at NRL.*

	Lab.	Generator	Type	ID[a] (cm)	OD[b] (cm)	Gas	References
1	NSWC[c]	Phoenix	Annular	3.35	3.65	Ar	Nolting *et al.*, 1995 Peterson & Weber, 1995 Weber & Fulghum, 1997*b* Weber *et al.*, 1997*a*
2	SNL	Saturn	Annular	1.5	3.5	Ar, Kr	Sanford *et al.*, 1996*a*
3	SNL	Saturn	Solid		4.5	Ar, Kr	Sanford *et al.*, 1996*a*
4	MPI	BJ5,[d] Ace4	Annular	3	4	Ar	
5	MPI	Ace4	Annular	4.2	5.8	Ar	Coleman *et al.*, 1997 Weber *et al.*, 1997*a*
6	MPI	Ace4	Annular	10.4	12.4	Ar	
7	MPI	Ace4	Solid		7	Ar	Coleman *et al.*, 1997 Weber *et al.*, 1997*a*
8	NRL	Hawk	Annular	1.9	2.1	Ne	Commisso *et al.*, 1998
9	NRL	Hawk	Annular	3.4	3.6	Ne	Commisso *et al.*, 1998
10	NRL	Hawk	Annular	4.9	5.1	Ne	Commisso *et al.*, 1998
11	MPI	Pithon	Annular	3.6	4.4	Ar	Coverdale *et al.*, 1996
12	MPI	Pithon	Annular	5.5	6.5	Ar	Coverdale *et al.*, 1996
12a				5.25	6.75		
13	MPI	DM2, DE, Saturn	Annular	4.2	5.8	Ar	Weber *et al.*, 1999*a*
14	MPI	DM2, DE, Saturn	Solid	1	7	Ar	Levine *et al.*, 1998 Weber *et al.*, 1998 Weber *et al.*, 1999*a* Moosman *et al.*, 1999*a* Levine *et al.*, 2001
15	MPI	Pithon, DE, Ace4	Annular	2	3	Ar	Deeney *et al.*, 1993 Coverdale *et al.*, 1996
16	MPI	DM2, DE	Solid	1	10	Ar	Levine *et al.*, 1998
17	MPI	DE, Saturn	2 shells	2, 6	4, 8	Ar, Kr	Sze *et al.*, 1999 Waisman *et al.*, 1999 Ingermanson *et al.*, 1999 Weber *et al.*, 1999b Song *et al.*, 2000
18	HCEI	GIT-12	2 shells	2.3, 5	3, 6	Ar	Shishlov *et al.*, 2000

[a]Inner diameter of the nozzle at the exit plane.
[b]Outer diameter of the nozzle at the exit plane.
[c]NSWC: Naval Surface Warfare Center, White Oak, MD, USA.
[d]Blackjack 5.

https://doi.org/10.1017/S026303460119405X Published online by Cambridge University Press

Contour plots of the gas distribution for a representative nozzle from each category is shown in Figure 12. In each case, the density distribution corresponds to typical argon-gas-fill parameters (pressure and timing) used in the corresponding PRS experiments. The density contours are derived using data like that in Figure 8. The qualitative nature of the gas flow and approximate density values are well represented by the contour plots. Contours are identified with the gas density in units of 10^{16} cm^{-3}. Low-density contours ($<10^{16}$ cm^{-3}) have been suppressed for visual clarity.

The annular nozzle depicted in Figure 12a (number 1 in Table 1) was used successfully on Phoenix (Nolting *et al.*, 1995). It has a narrow, short nozzle formed by concentric cones that produces a very hollow gas distribution at the nozzle exit. This nozzle has a large inward tilt angle (14°) and produces a highly divergent flow that increases the radial thickness of the shell with distance from the nozzle. The combination of the divergence and inward tilt result in a distribution that is peaked on axis, 3–4 cm from the nozzle. Though very annular close to the nozzle, this type of

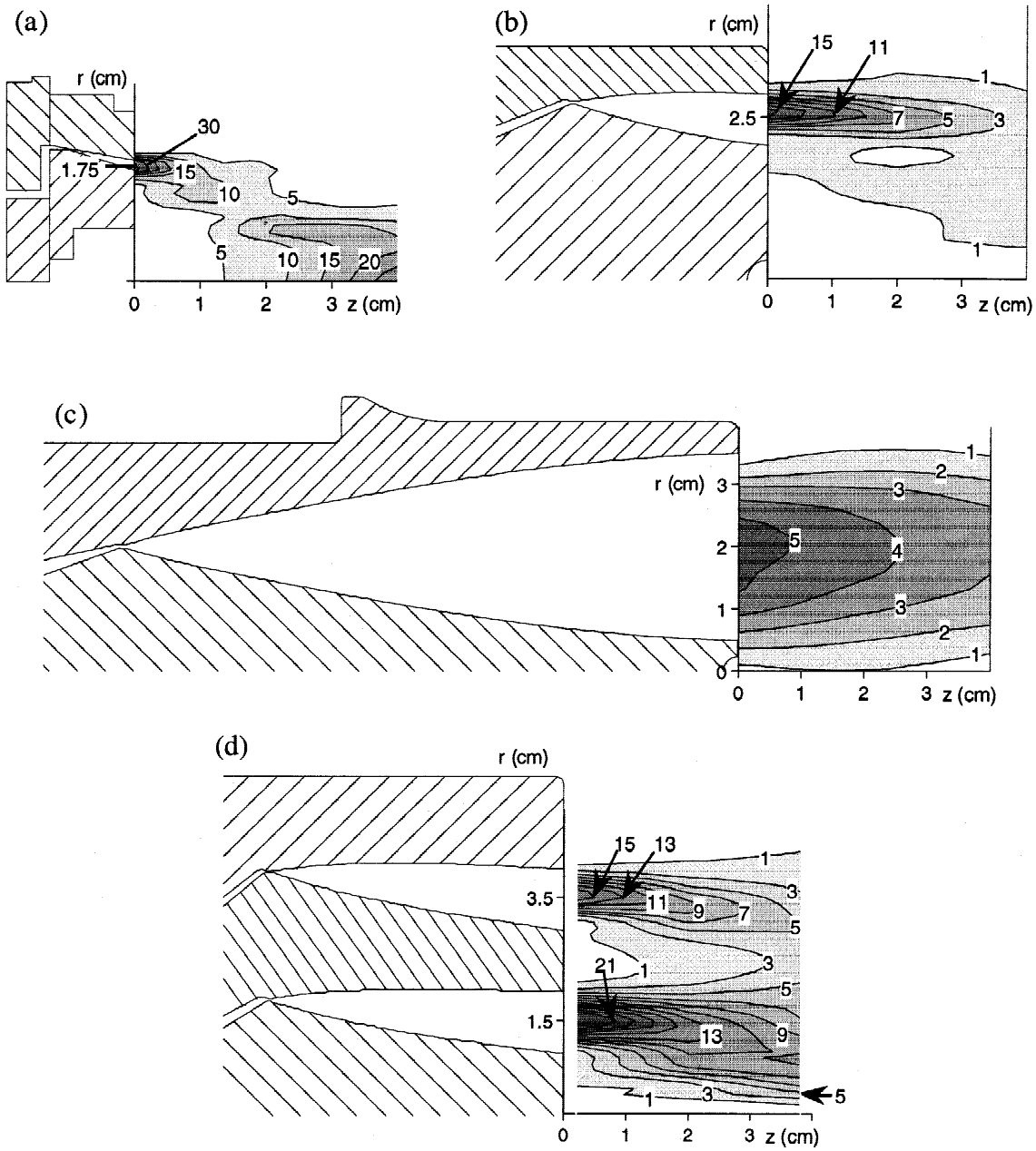

Fig. 12. Sample nozzle *r*–*z* cross sections and measured gas-distribution contours for: (1) single-shell nozzles [(a) Phoenix 3.5-cm diameter and (b) MPI 5-cm diameter]; (2) "Solid" fill nozzle [(c) MPI 7-cm diameter]; and (3) double-shell nozzle [(d) MPI SOS]. Argon density contours are denoted in units of 10^{16} cm^{-3}.

https://doi.org/10.1017/S026303460119405X Published online by Cambridge University Press

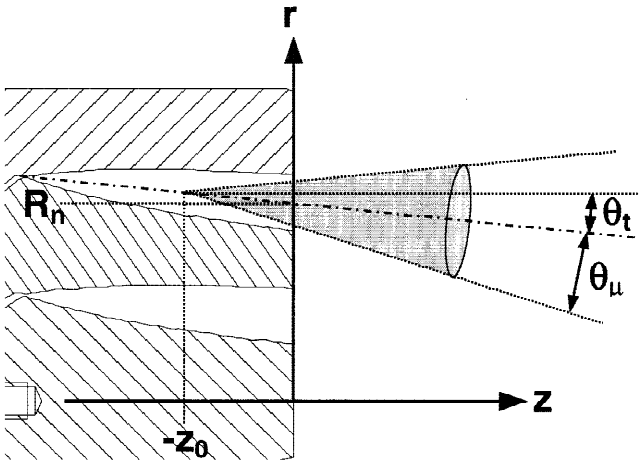

Fig. 13. Ballistic-gas-flow model parameter definitions overlaid on the MPI SOS nozzle geometry.

nozzle creates gas distributions that have a strong two-dimensional nature.

A more conventional single-shell annular nozzle is represented by the MPI 5-cm nozzle used on Decade Module 2 (DM2), Double Eagle (DE) and Saturn, shown in Figure 12b (number 13 in Table 1). The nozzle is longer and more contoured than the Phoenix nozzle to produce a high Mach-number flow, but by necessity produces thicker shells close to the nozzle. The divergence is noticeably less than for the Phoenix nozzle.

Solid-fill nozzles with more uniformly distributed gas distributions are being considered as a way to mitigate instabilities during implosions from large initial radii. A representative example is the PI 7-cm diameter solid-fill nozzle shown in Figure 12c (number 14 in Table 1). Most of the 7-cm diameter is filled with gas and the flow is relatively straight and well confined.

The double-shell MPI SOS nozzle in Figure 12d (number 17 in Table 1) is the nozzle used above to illustrate the gas measurement technique. These density contours are derived using the data in Figure 8. This nozzle can produce a variety of gas distributions by independently varying the pressures in the two plenums.

These measurements illustrate the variety of parameters that can be obtained using high-sensitivity interferometry. The following sections describe how this information is used to make physical, analytic fits to the gas distributions, to perform snowplow implosions using these fits, and to estimate the *K*-shell X-ray yield. The power of this approach is its potential to predict realistic operating conditions that will optimize the *K*-shell radiation from a given nozzle geometry and to suggest changes in geometry that will further improve performance.

3. BALLISTIC-GAS-FLOW MODEL

The ballistic-gas-flow model (BFM; Mosher *et al*., 1999) treats flow from a gas-puff nozzle as emanating from an imaginary thin annulus of radius R_0 with a Gaussian distribution in polar angle θ_μ about a nozzle tilt angle θ_t and propagates the distribution ballistically forward in z. The geometry is shown in Figure 13 for the MPI SOS nozzle. The annulus is set back from the face of the nozzle at $z = 0$ by a distance z_0 to account for the width of the density distribution at the nozzle face. The center line of the divergence cone passes through the nozzle face at radius $R_n = R_0 - \theta_t z_0$.

The BFM distribution can be derived with the aid of Figure 14. For local cartesian coordinates with origin on the emission annulus at $(R_0, \phi, -z_0)$ as shown, the gas is emitted in an angular Gaussian probability distribution P given by

$$\frac{dP}{d\Omega} = \frac{1}{\pi\theta_\mu^2} \exp\left[-\frac{\theta_x^2 + (\theta_y + \theta_t)^2}{\theta_\mu^2}\right], \tag{5}$$

where $d\Omega$ is an element of solid angle. The angular distribution can be referred to the point $(r, 0, z)$ at which $n(r, z)$ is to be evaluated using the small-angle relations

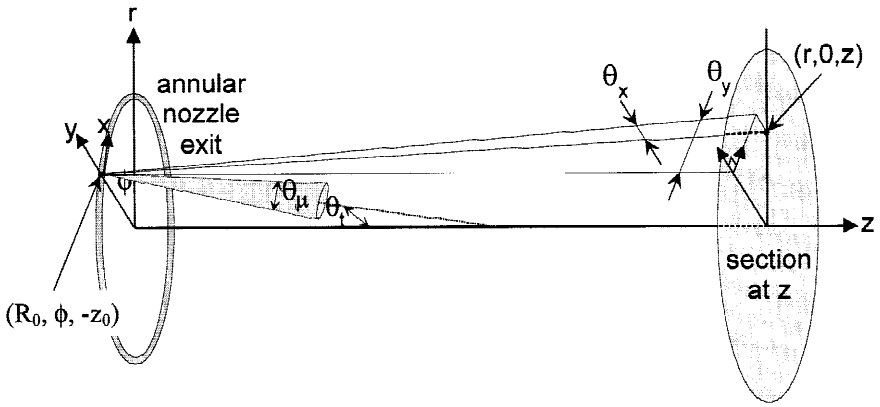

Fig. 14. Ballistic-gas-flow model coordinate geometry.

https://doi.org/10.1017/S026303460119405X Published online by Cambridge University Press

$$\theta_x = \frac{r\sin\phi}{z+z_0}; \qquad \theta_y = \frac{r\cos\phi - R_0}{z+z_0}. \tag{6}$$

The density at (r, z, t) is determined from the line density $N(1/\text{cm}) = m/m_{\text{Ar}}$ emitted at the face of the nozzle at time $t - z/V_g$ (Sect. 2.3), where V_g is the flow velocity of the gas. The contribution to $n(r, z)$ over area dA due to the increment $dN = Nd\phi/2\pi$ emitted at $(R_0, \phi, -z_0)$ is

$$dn = dN\frac{dP}{dA} = \frac{Nd\varphi}{2\pi(z+z_0)^2}\frac{dP}{d\Omega}. \tag{7}$$

Substituting from Eqs. (5) and (6), and integrating Eq. (7) over ϕ leads to

$$n(r,z) = \frac{N}{\pi\delta^2}\exp\left[-\frac{r^2+R_z^2}{\delta^2}\right]I_0\left(\frac{2rR_z}{\delta^2}\right), \tag{8}$$

where $R_z(z) = R_n - z\theta_t$ is the radius of the divergence cone center line at z, $\delta(z) = (z+z_0)\theta_\mu$ measures the radial width of the divergence cone at z, and I_0 is the modified Bessel function of zero order.

The shapes of ballistic model density profiles at various axial locations are specified by the single parameter δ/R_z. The dependence of shape on this parameter is shown in Figure 15. For $\delta/R_z \ll 1$, the radial density distribution is a thin Gaussian annulus centered about R_z. For $\delta/R_z > 1$, that is, for $z + z_0 > R_0/(\theta_\mu + \theta_t)$, the profile approaches a Gaussian of width δ about the axis of symmetry.

With the distribution defined by Eq. (8), the gas density at any point $n(r, z)$ can be determined once the parameters R_n, z_0, θ_t, θ_μ, and N are chosen for a given nozzle and flow time. Values for the tilt angle and R_n are constrained by the nozzle geometry. The line density N depends weakly on z because of the time variation of mass emitted at the nozzle face (Sect. 2.3) and time of flight to z. The line density is determined at discrete axial locations from Eq. (4). A linear interpolation between these points results in $N(z)$ for the BFM distributions. The two free parameters z_0 and θ_μ are then chosen to provide the best overall fit to the measured density profiles at all z values simultaneously.

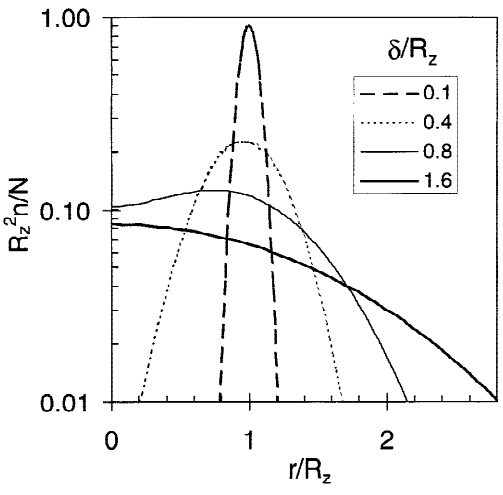

Fig. 15. Ballistic-gas-flow model radial profiles for various values of δ/R_z.

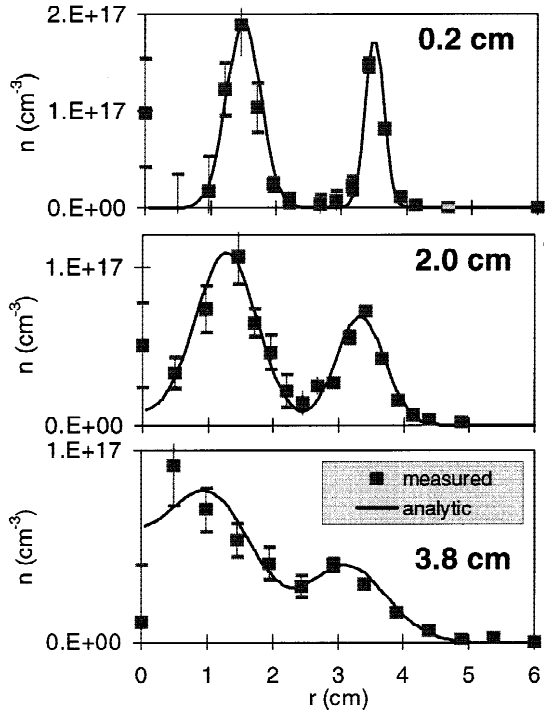

Fig. 16. Comparison of interferometer-measured and BFM radial profiles at three axial locations for the MPI SOS nozzle operating at a 500-μs flow time with 10 psia in each plenum.

Figure 16 compares interferometer-measured (points) and ballistic-model-fit (curves) density profiles at three axial locations for the DE SOS nozzle operating at a 500-μs flow time with 10 psia in each nozzle. Table 2 shows ballistic-model-fit parameters for separately measured density distributions from the inner and outer nozzle. The BFM density plotted in Figure 16 is the sum of the BFM fits to each nozzle. Equally good fits to 400-μs flow-time data were

Table 2. *Ballistic-model parameter fits to separately measured density distributions from the inner and outer nozzle for the profiles shown in Figure 16.*

	z (cm)	Inner	Outer	Notes
z_0 (cm)		2.14	0.91	fit
θ_μ (rad)		0.157	0.1806	fit
θ_t (rad)		0.087	0.087	geometric
R_n (cm)		1.54	3.53	geometric
N (1/cm)	0.2	1.5E+18	2.0E+18	measured
N (1/cm)	2	1.3E+18	1.8E+18	measured
N (1/cm)	3.8	1.1E+18	1.5E+18	measured

https://doi.org/10.1017/S026303460119405X Published online by Cambridge University Press

achieved using the same values of R_n, z_0, θ_t, and θ_μ. This suggests that these BFM parameters are descriptors for the nozzles, and may be used to characterize density distributions at other axial locations and for other flow times.

Use of the BFM density distribution has a number of advantages over use of the piece-wise interferometry-measured distribution to which it is fit. The model provides an easy, physical means to interpolate radial density distributions between axial measurement locations for finer-zoned two-dimensional MHD calculations. The model provides $n(r, z)$ for a range of pressures and plasma-flow times by changing only $N(z)$. In addition, it can be used as a design tool by varying BFM parameters to determine how changes in the nozzle may alter load dynamics on a given z-pinch driver (to optimize distributions for maximum K-shell yield, reduce zippering, etc.), and to provide realistic puff-gas loads for modeling future experiments on various z-pinch drivers.

4. KINEMATICS OF DISTRIBUTED-MASS IMPLOSIONS

To better understand the implosion dynamics of PRS loads with radial mass distributions, consider first the simple slug model for the implosion of a zero-thickness annulus of mass m(g/cm) and initial radius R_0. The force equation takes the form

$$m\frac{d^2R}{dt^2} = -\frac{I^2(t)}{100R(t)}, \tag{9}$$

for radius R (cm), time t (s), and pinch current I (A). Equation (9) is doubly integrated in time until a selected stagnation radius R_f is reached at implosion time t_{imp}. Multiplying Eq. (9) by the implosion velocity $V(t) = dR/dt$ and integrating provides the implosion kinetic energy K at stagnation:

$$K\,(\mathrm{J/cm}) = \frac{10^{-7}}{2}\,mV_f^2 = -10^{-9}\int_0^{t_{imp}}\left(\frac{I^2}{R}\frac{dR}{dt}\right)dt, \tag{10}$$

where $V_f = V(t_{imp})$. This form can also be derived by considering the electrical power into the time-varying inductance of the imploding plasma:

$$L\,(\mathrm{H/cm}) = 2\times10^{-9}\ln\left(\frac{R_w}{R(t)}\right), \tag{11}$$

where R_w is the return-current radius. The total energy flowing into the load region is

$$\int_0^{t_{imp}} I\frac{d}{dt}(LI)dt = \int_0^{t_{imp}}\left(\frac{1}{2}I^2\frac{dL}{dt}\right)dt + \Delta\left(\frac{1}{2}LI^2\right). \tag{12}$$

The second term on the right-hand side is the change in magnetic energy around the imploding load, so the that the first term is the work done on the plasma E_W (J/cm):

$$E_W = \frac{1}{2}\int_0^{t_{imp}} I^2\frac{dL}{dt}\,dt. \tag{13}$$

E_W is identical to K when Eq. (11) is substituted for L. Equation (13) is the work done on the plasma in general, and also holds for distributed-mass distributions for which the current-flow radius is well defined. Note that E_W depends most strongly on the current near the end of the implosion where dL/dt is largest.

The simplest distributed load is a nested pair of annuli, defined by masses m_1 and m_2 initially at R_1 and $R_2 < R_1$. Current initially flows in the outer annulus, achieving velocity V_1 at time t_1 when m_1 collides with the stationary mass m_2 at radius R_2. For an inelastic collision, the total mass $m = m_1 + m_2$ subsequently carries the current to stagnation in accordance with Eq. (9). The velocity V of the total mass at t_1 is determined from conservation of momentum during the collision: $V(t_1) = m_1V_1(t_1)/m$. Internal energy $E_{int} = m_1V_1^2(t_1)/2 - mV^2(t_1)/2$ due to shock heating at collision is thus created. If this internal energy is not radiated away during the remainder of the implosion, energy balance at stagnation requires $E_W(t_{imp}) = K(t_{imp}) + E_{int}$. This nested-annuli example demonstrates that the work done on the plasma always exceeds the implosion kinetic energy when the mass is not distributed in a single thin annulus.

For continuously distributed gas-puff density distributions, the implosion kinematics are most simply described by radial snowplow implosions in which the pinch current flows in a thin layer at radius R, so that

$$\frac{d}{dt}\left[\Delta m(R)\frac{dR}{dt}\right] = -\frac{I^2}{100R}. \tag{14}$$

Here, $\Delta m(R)$ is the mass swept up by the magnetic piston between an initial discharge-breakdown radius R_0 and $R(t)$:

$$\Delta m(R) = 2\pi\int_R^{R_0}\rho r\,dr, \tag{15}$$

where ρ (g/cm^3) is the radial mass-density distribution of the initial gas puff. In what follows, Eq. (14) is doubly integrated in time until R reaches R_f at $t = t_{imp}$ using ρ from BFM distributions at selected axial locations (Mosher *et al.*, 1999).

As in the slug-model example above, Eq. (14) can be multiplied by dR/dt and integrated over time, to yield

$$K + \int_0^{t_{imp}}\frac{1}{2}\left(\frac{dR}{dt}\right)^2\left(\frac{d\Delta m}{dt}\right)dt = E_W. \tag{16}$$

The middle term can be identified as the internal energy continuously created by shock heating in the accreting-mass layer at the imploding magnetic piston. If the internal energy is not radiated away during implosion, it should contribute to heating of, and radiation from, the stagnated plasma.

https://doi.org/10.1017/S026303460119405X Published online by Cambridge University Press

Radial snowplow implosions in BFM density distributions were carried out at various axial positions for representative shots of the DE SOS experiment (Sze *et al*., 1999). All of the shots used 4-cm-long argon loads with the nozzle-output plane at the cathode. The inner and outer nozzle pressures were adjusted to achieve various radial distributions over a range of implosion times. The BFM density distributions for each analyzed shot were determined by scaling the inner- and outer-nozzle line densities shown in Table 2 by the corresponding shot pressures divided by 10 psia.

For the implosion computations, measured current histories for each shot, rather than a circuit model, were employed. For each axial location z, an initial radius $R_0(z)$ for current flow was chosen by assuming breakdown at 1×10^{13} cm^{-3} argon density on the outside of the distribution. Increasing the breakdown density by a factor of ten, with a corresponding decrease in initial radii, did not significantly change the implosion times $t_{imp}(z)$. Consistency between the experiment and analyses of the modeled shots was then determined by comparing the range of computed t_{imp} values with the timing of the measured *K*-shell radiation pulse. Figure 17 shows an example of this analysis for implosions near the cathode (nozzle plane) at $z = 0.2$ cm, at the center of the 4-cm-long pinch, and near the anode at 3.8 cm, along with the measured *z*-pinch current and *K*-shell radiation pulse. The figure demonstrates that the computed implosion times are consistent with the BFM density distribution, current pulse, and *K*-shell radiation signal. For these computations, stagnation is assumed at a radius $R_f = 0.25$ cm, a value comparable to the outside radius of *K*-shell pinhole images (Fig. 20). For all of the Double Eagle nested-shell distributions examined, anode-side snowplows are computed to implode earlier than those nearer the cathode, even though anode-side implosions start from larger radius. This is due to the lower line densities and more diffuse distributions that occur with increasing z.

The implosion behavior shown in Figure 17 is mirrored in 2-D MHD DELTA code simulations of nested argon shell implosions using BFM density distributions (Waisman *et al*., 1999). For this application, the unstructured triangular-mesh DELTA code was run in Eulerian mode with one temperature, a coronal-radiative equilibrium equation of state, and Spitzer resistivity at the average ionization state. Such 2-D modeling is required to self-consistently include Rayleigh–Taylor-instability, axial-motion, and internal-plasma-state effects on the implosion dynamics, though some of these phenomena have been modeled with a 2-D snowplow model (Shishlov *et al*., 2000). Figure 18 shows three snapshots in time from the 2-D MHD computation that demonstrate a change in the tilt of the current path midway through the implosion. As in the Figure 17 snowplow calculations, the current-path boundaries at early times tilt outward towards the anode, following the spreading gas-puff distribution. Later in time, the tilt changes direction due to higher anode-side

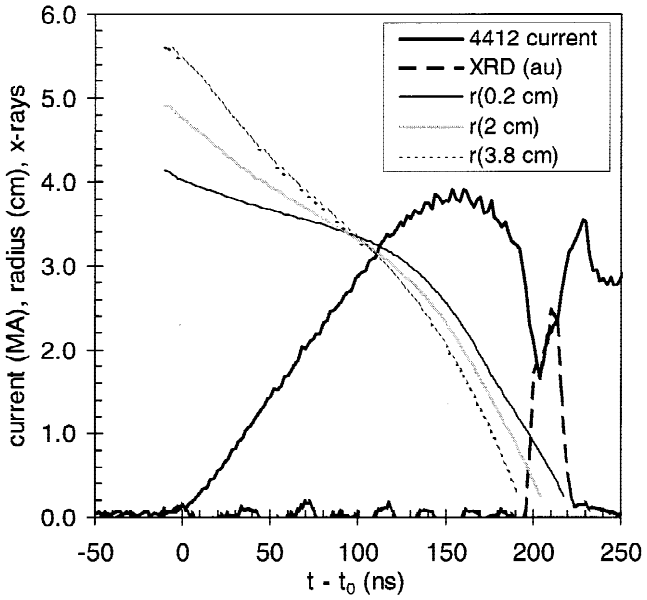

Fig. 17. Shot 4412 load-current and K-shell-radiation pulses along with computed snowplow-implosion radii at three axial locations.

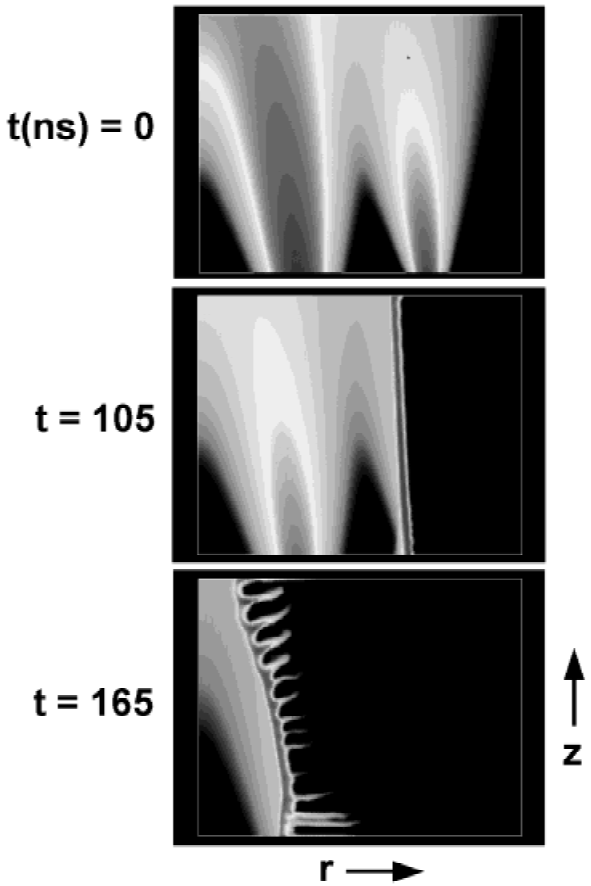

Fig. 18. Two-dimensional MHD computations for the conditions of shot 4428 using BFM fits to the initial density distribution. For each figure, the nozzle is at bottom.

https://doi.org/10.1017/S026303460119405X Published online by Cambridge University Press

velocities in the more diffuse, lower-mass distributions, resulting in anode-to-nozzle zippering at stagnation. Similar current-channel dynamics has been observed in recent single-nozzle (similar to Fig. 12a) neon-implosion experiments conducted on the NRL Hawk driver using an Alameda Applied Science Corp. (AASC) shearing interferometer (Qi *et al.*, 2002).

For both the snowplow and MHD calculations, implosion occurs first at the anode and progresses over 20 ns to the nozzle. Though observed on 400-μs flow time shots, this prediction does not agree with the timing of axially resolved PIN-diode-array measurements on 500-μs flow-time shots. Mechanisms associated with subtleties of gas flow not captured by interferometry, nonuniform preionization (Sect. 2.4), and instability effects are being considered to resolve this discrepancy. Even so, the measured axial variation of *K*-shell yield from this diagnostic is shown below to agree with the analysis.

5. *K*-SHELL RADIATION YIELD FROM SNOWPLOW IMPLOSIONS

The *K*-shell yield can be estimated from a simple two-level radiation-scaling model (Mosher *et al.*, 1998) requiring input of the implosion energy at stagnation, the stagnation radius, and the line mass. Snowplow implosions provide the stagnation energy $E_W(z)$ at various axial locations of the BFM mass distributions. Alternately, the implosion kinetic energy $K(z)$ can be calculated from $mV_f^2/2$ at each axial location. Results of energy computations for the shot of Figure 17 are shown in Figure 19. About a 50% increase in E_W is computed as z increases from nozzle to anode. The roughly 5-kJ/cm difference between E_W and K is due to the creation of internal energy. The dotted curve in Figure 19 is discussed at the end of this section. The local line mass $m(z)$ derives from the ballistic-model density distributions associated with the shot nozzle pressures, as described in Section 3. The axial variations of E_W and m were then used to estimate the argon *K*-shell yield per centimeter dY/dz (J/cm) from the two-level model assuming a constant 0.25-cm stagnation radius.

Results of the radiation calculations are shown in Figure 20 for the implosions of Figure 17, where they are compared with axially resolved PIN-diode-array measurements for the same shot. This zipper diagnostic uses a linear array of 14 silicon PIN diodes that are positioned behind a perpendicular slit to provide a time-resolved record of *K*-shell emission as a function of distance along the pinch (Coleman *et al.*, 1999). In general, the sum of the zipper-diode signals agrees well with the *K*-shell power waveforms measured with total-pinch-viewing XRDs and PCDs, and 1-D "pictures" of implosions derived from time-integrated zipper data agree well with 2-D pinhole images. For comparison with the dY/dz prediction of Figure 20, the zipper data were time integrated and summed in 1-cm increments along the pinch.

Both measurements (dash-dot) and modeling (solid) in Figure 20 show an increase in local yield as z increases, a trend generally observed during the DE SOS experiment. The dot-

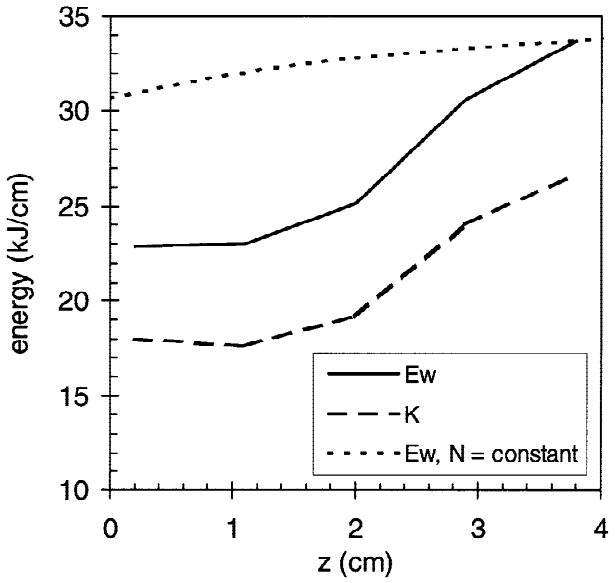

Fig. 19. Variation of total implosion energy (solid) and kinetic energy (dashed) with axial position for shot 4412. The dotted line shows the variation of energy when the mass is everywhere reduced to the value at 3.8 cm.

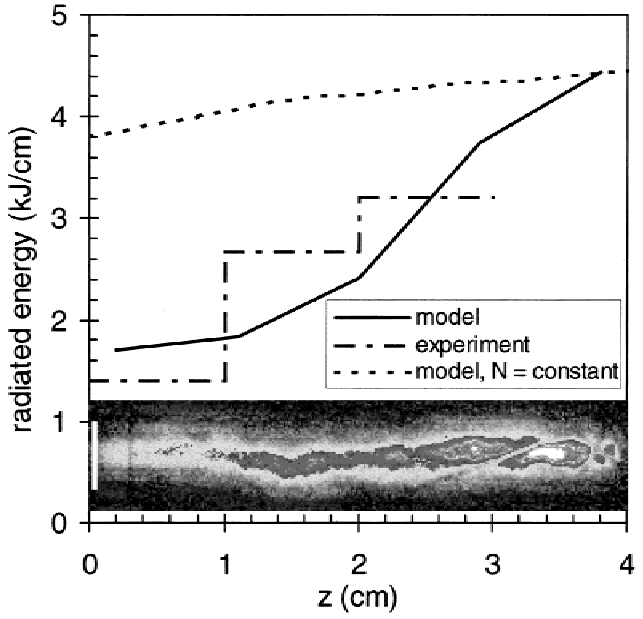

Fig. 20. Calculated *K*-shell yield versus axial position (solid) compared to axially resolved PIN-diode-array measurements (dot-dash) for the implosions of Figure 17. A time-integrated *K*-shell pinhole image for that shot with a 0.5-cm-long bar is shown to the axial scale of the plot. The dotted line shows the calculated variation of radiation when the mass is everywhere reduced to the value at 3.8 cm.

https://doi.org/10.1017/S026303460119405X Published online by Cambridge University Press

ted curve is discussed at the end of this section. The time-integrated X-ray pinhole image for the shot with a 0.5-cm-long scale bar is shown to the axial scale of the plot. The (false gray-scale) intensity distribution of the image confirms the plotted increase in radiation away from the nozzle and the ~0.25-cm radius for X-ray emission. In the two-level calculation, dY/dz increases with z because E_W does. Thus, the observed yield increase with z may not be primarily a manifestation of 2-D instability effects, but may be associated with larger implosion energies for the anode-side distributions. Instability mediation provided by the distributed-mass load may have permitted the 1-D energetics advantage of the anode-side distributions to be expressed. Conversely, single-nozzle experiments have demonstrated reduced *K*-shell radiation close to the nozzle attributed to the higher R-T instability levels of annular distributions (Coleman & Levine, 1999). In support of this view, good X-ray-yield performance for diffuse distributions from widely dispersed single nozzles has been demonstrated in recent 5-cm-diameter neon gas-puff experiments on Hawk (Moosman *et al.*, 1999*b*). Thus, both 1-D and 2-D mechanisms may be responsible for the observed yield per centimeter increase with z.

The 11.3-kJ integral of the two-level dY/dz over z from Figure 20 is well matched to the 11.7-kJ *K*-shell yield on this shot measured with a *K*-shell-filtered XRD. Using R_f = 0.25 cm, similar agreement between computed and measured yields was obtained on other analyzed shots for which the computed implosion time agreed with that observed. When z-averaged values of E_W and m are used in the two-level model for these shots, the single value of calculated yield also agrees well with the integral under dY/dz and the measured yield. This agreement provides a means to estimate the two-level yield for the full shot series using only z-averaged masses derived from the shot nozzle pressures and the BFM distributions, and z-averaged implosion energies scaled from the peak shot current I_m: $\langle E_W\ (\mathrm{kJ/cm})\rangle = 1.9 I_m^2\ (\mathrm{MA})$. Results of these calculations are shown in Figure 21 as a function of implosion time and are compared to the corresponding XRD-measured yields for the Double Eagle test series. Calculated yields based on E_W are seen to reproduce the experimental trends. The yield computations were repeated using the kinetic energy at stagnation *K* rather than E_W. The predicted *K*-shell yields using *K* are well below the experimental values, suggesting that internal energy contributes to radiation excitation at stagnation.

The measurements and analyses presented here can be used to assess possible improvements in X-ray performance due to modified gas-puff-nozzle characteristics. Consideration is limited to modifications that will not invalidate either the BFM or implosion parameters found to fit the experiment. For example, increasing the outer nozzle radius R_n may lead to increased R-T disruption of the implosion, resulting in an unpredictable change in the effective R_f, the value of which conforms with X-ray pinhole measurements and agreement between two-level modeling and yield measurements. One modification suggested by both the 1-D analysis and experiment would be to preserve R_n, θ_t, and θ_μ, but choose a constant line density N along the full length of the pinch equal to the measured value at 3.8 cm. In 1-D, such a change would reduce implosion-time zippering and increase implosion energy near the nozzle. In addition, argon gas-puff experiments and associated 2-D MHD computations indicate an improvement in implosion quality with reduced zippering due to reduced axial flow (Deeney *et al.*, 1993). In practice, this change might most easily be achieved by replacing the present gas-puff valve with one faster opening, so that the generator fires on the $m(t)$ plateau. An example of such a valve developed by AASC was tested at NRL using nozzle number 2 in Table 1. The fast valve reduced the argon gas rise time from 300 μs to 100 μs and would produce constant N conditions about 150 μs after the gas starts to emerge from the nozzle, a reasonable timing for PRS experiments.

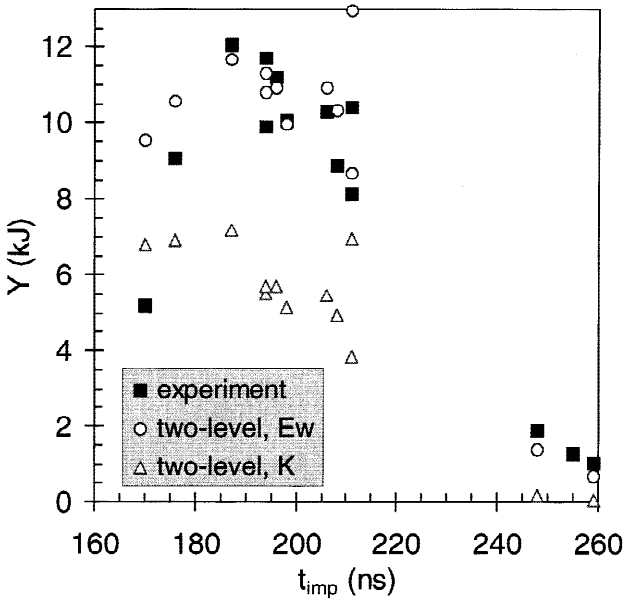

Fig. 21. Two-level *K*-shell yield as a function of implosion time using either the work done on the plasma or kinetic energy as the stagnation energy compared to the corresponding XRD-measured yields for the SOS Double Eagle test series.

Results of the 1-D modeling with this constant N modification are shown by the dotted curves of Figures 19 and 20. Increased implosion energy results from decreasing anode-to-nozzle zippering to about 5 ns. The associated increase in dY/dz results in a calculated 48% increase in total yield above that with the previously discussed $N(z)$. The dramatic improvement suggested by the idealistic 1-D computation may not be realized because of persistent nozzle-side R-T instability. An additional design improvement that does not compromise modeling parameters is extending the anode to 6 cm from the nozzle and defining a new cathode by a transparent wire mesh about 2 cm from the nozzle face. Such a modification has been found to boost cathode-side

https://doi.org/10.1017/S026303460119405X Published online by Cambridge University Press

K-shell radiation by eliminating the single-nozzle R-T-unstable annular distribution from the load region (Coleman & Levine, 1999). For this modification, the BFM can be used for analysis with $z = 2–6$ cm.

6. CONCLUSIONS

Density distribution measurements using a high-sensitivity two-color laser interferometer have been reviewed for a wide variety of gas-puff PRS *z*-pinch experiments. These accurate gas-distribution measurements are required for determining experimental load parameters, modeling implosion dynamics, understanding the radiation properties of the stagnated pinch, and for predicting PRS performance in future experiments. Gas distributions have been measured from four general nozzle categories: single shells with shaped high-Mach-number nozzles, single shells with short, narrow nozzles, nozzles designed to produce "solid" (well filled-in) gas distributions, and double-shell nozzles. In addition to the neutral-gas *r*–*z* distribution, measurements of azimuthal symmetry and ionization produced by a UV flashboard source have been reviewed. Interferometry measurement and analysis techniques were exemplified using data obtained with the MPI double-shell nozzle fielded on DE and the SNL Saturn generator. This nozzle was chosen as an example because its density distribution is more complex than for other cases, and because modeling based on the gas-distribution measurements has been benchmarked against the DE experiments.

A simple ballistic-gas-flow model was shown to provide good physics-based analytic fits to the measured *r*, *z* density distributions. These BFM fits provide a convenient means to smoothly interpolate radial density distributions between discrete axial measurement locations for finer-zoned two-dimensional MHD calculations. The BFM has also been used to determine how changes in nozzle parameters and load geometry might alter implosion dynamics and radiation performance. The utility of the BFM was demonstrated in an analysis of the MPI shell-on-shell gas-puff experiments on Double Eagle. For the analysis, radial snowplow computations at various axial locations were combined with a two-level radiation model to predict the *K*-shell yield as a function of *z*. Both this analysis and the experiment show increased yield per centimeter with increased distance from the nozzle, suggesting that modified gas-puff-nozzle characteristics may achieve an increase in overall *K*-shell yield by boosting yield per centimeter close to the nozzle. Simple nozzle modifications were suggested that resulted in a substantial calculated yield increase.

The snowplow and radiation-scaling analyses provided a technique for predicting the *K*-shell yield for the full shot series of the DE SOS experiment using only summary spreadsheet information. Predicted yields agree with measurements over the range of experimental implosion times and demonstrate the importance of accurate density-distribution data. This agreement also demonstrates the ability of simple implosion and radiation models using this data to aid in the design of, and to predict performance of, gas-puff loads on future experiments.

ACKNOWLEDGMENTS

Various parts of the work reported here were supported by the U.S. Defense Threat Reduction Agency (DTRA), Sandia National Laboratories and the Naval Surface Warfare Center, White Oak, MD. Contributions to experiments and helpful discussions are appreciated from J. Riordan, MPI; S. Stephanakis, D. Black, and G. Peterson, NRL; C. Coverdale, R. Spielman, and T. Sanford, SNL; D. LePell, Ktech Corp.; and H. Murphy, Science Applications International Corp. Thanks also to D. Bell, DTRA, for support during preparation of this article.

REFERENCES

Baksht, R.B. *et al.* (1997). *Plasma Phys. Rep.* **23**, 195.
Coleman, P. & Levine, J. (1999). *IEEE Conference Record—Abstracts*, 1999 Int. Conf. Plasma Science, Monterey, CA. p. 298. IEEE Catalog No. 99CH36297, IEEE Service Center, Piscataway, NJ.
Coleman, P. *et al.* (1997). *Proc. Fourth Int. Conf. Dense Z Pinches*, Vancouver, AIP Conf. Proc. 409, p. 119. New York: American Institute of Physics.
Coleman, P. *et al.* (1999). Abstract CO16. *Bull. APS* **44**, 53.
Commisso, R.J. *et al.* (1998). *IEEE Trans. Plasma Sci.* **26**, 1068.
Coverdale, C. *et al.* (1996). *Bull. APS* **41**, 1468.
Deeney, C. *et al.* (1993). *Phys. Fluids B* **5**, 992.
Deeney, C. *et al.* (1995). *Phys. Rev. E* **51**, 4823.
Deeney, C. *et al.* (1998). *Phys. Rev. Lett.* **81**, 4883.
Gol'berg, S.M. & Velikovich, A.L. (1993). *Phys. Fluids B* **5**, 1164.
Hammer, J.H. *et al.* (1996). *Phys. Plasmas* **3**, 2063.
Ingermanson, R. *et al.* (1999). Abstract CO17. *Bull. APS* **44**, 53.
Levine, J. *et al.* (1998). *Proc. Twelfth Int. Conf. High-Power Particle Beams*, Haifa, Israel, p. 95. IEEE Catalog No. 98EX103, IEEE Service Center, Piscataway, NJ.
Levine, J.S. *et al.* (2001). *Phys. Plasmas* **8**, 533.
Moosman, B. *et al.* (1999*a*). *Rev. Sci. Instrum.* **70**, 672.
Moosman, B. *et al.* (1999*b*). *Bull. APS* **44**, 105.
Mosher, D. (1994). *Proc. Tenth Int. Conf. on High-Power Particle Beams*, San Diego, CA, NTIS PB95-144317, p. 159.
Mosher, D. *et al.* (1998). *IEEE Trans. Plasma Sci.* **26**, 1052.
Mosher, D. *et al.* (1999). *Proc. Twelfth IEEE Int. Pulsed Power Conf.*, Monterey, CA, IEEE Cat. No. 99CH36358, p. 1078.
Nolting, E. *et al.* (1995). *IEEE Conference Record—Abstracts*, 1995 Int. Conf. Plasma Science, Madison, WI, p. 207. IEEE Catalog No. 95CH35796, IEEE Service Center, Piscataway, NJ.
Peterson, G.G. & Weber, B.V. (1995). *IEEE Conference Record—Abstracts*, 1995 Int. Conf. Plasma Science, Madison, WI, p. 207. IEEE Catalog No. 95CH35796, IEEE Service Center, Piscataway, NJ.
Qi, N. *et al.* (2002). to be published in *IEEE Trans. Plasma Sci.* **30**.
Rousskikh, A.G. *et al.* (1999). *Plasma Phys. Rep.* **25**, 579.
Sanford, T.W.L. *et al.* (1996*a*). *IEEE Conf. Record—Abstracts*, 1996 IEEE Int. Conf. Plasma Sci., p. 251. IEEE Catalog No. 96CH35939, IEEE Service Center, Piscataway, NJ.
Sanford, T.W.L. *et al.* (1996*b*). *Phys. Rev. Lett.* **77**, 5063.

https://doi.org/10.1017/S026303460119405X Published online by Cambridge University Press

Shishlov, A.V. *et al.* (2000). *Phys. Plasmas* **7**, 1252.
Song, Y. *et al.* (2000). *Rev. Sci. Instrum.* **71**, 3080.
Spielman, R.B. *et al.* (1997). *Proc. Fourth Int. Conf. Dense Z Pinches*, Vancouver, AIP Conf. Proc. 409, p. 101. New York: American Institute of Physics.
Sze, H. *et al.* (1999). Abstract CO18. *Bull. APS* **44**, 53.
Thornhill, J.W. *et al.* (1996). *J. Appl. Phys.* **80**, 710.
Velikovich, A.L. *et al.* (1998*a*). *Phys. Rev. Lett.* **77**, 853.
Velikovich, A.L. *et al.* (1998*b*). *Phys. Plasmas* **5**, 3377.
Waisman, E. *et al.* (1999). Abstract CO110. *Bull. APS* **44**, 53.
Weber, B.V. & Fulghum, S.F. (1997). *Rev. Sci. Instrum.* **68**, 1227.
Weber, B.V. *et al.* (1997). *Proc. Fourth International Conf. Dense Z Pinches*, Vancouver, AIP Conf. Proc. 409, p. 459. New York: American Institute of Physics.
Weber, B.V. *et al.* (1998). *Proc. Twelfth Int. Conf. High-Power Particle Beams*, Haifa, Israel, p. 342. IEEE Catalog No. 98EX103, IEEE Service Center, Piscataway, NJ.
Weber, B.V. *et al.* (1999*a*). *Rev. Sci. Instrum.* **70**, 687.
Weber, B.V. *et al.* (1999*b*). *Bull. APS* **44**, 104.

https://doi.org/10.1017/S026303460119405X Published online by Cambridge University Press